Journal of Computational Physics 228 (2009) 7543–7564

Contents lists available at ScienceDirect

Journal of Computational Physics

journal homepage: www.elsevier.com/locate/jcp

Stability analysis of a predictor/multi-corrector method for staggered-grid Lagrangian shock hydrodynamics ☆

E. Love, W.J. Rider, G. Scovazzi *

1431 Computational Shock- and Multi-physics Department, Sandia National Laboratories, P.O. Box 5800, MS 1319, Albuquerque, NM 87185-1319, USA

ARTICLE INFO

Article history:
Received 2 March 2009
Received in revised form 5 June 2009
Accepted 26 June 2009
Available online 22 July 2009

Keywords:
von Neumann stability analysis
Predictor/multi-corrector algorithm
Mid-point time integrator
Lagrangian shock hydrodynamics
Staggered formulation

ABSTRACT

This article presents the complete von Neumann stability analysis of a predictor/multi-corrector scheme derived from an implicit mid-point time integrator often used in shock hydrodynamics computations in combination with staggered spatial discretizations. It is shown that only even iterates of the method yield stable computations, while the odd iterates are, in the most general case, unconditionally unstable. These findings are confirmed by, and illustrated with, a number of numerical computations. Dispersion error analysis is also presented.

1. Introduction

The present article proposes a complete von Neumann stability and dispersion analysis of a linearized version of the time-integration algorithm presented in [17,18]. This approach is based on a predictor/multi-corrector variant of the implicit mid-point time integrator, and has the appealing property of conserving mass, momentum and total energy in the nonlinear setting, without staggering *in time* the thermodynamic variables with respect to the kinematic variables. The algorithm exactly corresponds to the staggered (in space) finite difference formulations of [2,5] in the case of one spatial dimension and periodic boundary conditions. Recently, the authors have discovered that the algorithm in [2,3,5,17,18] *does not* yield stable solutions in the case of an odd number of iterations [13], and the present work is a documentation of the detailed analysis that followed these initial observations.

The von Neumann analysis of stability is well established for Lagrangian schemes [10,21], and, in this context, we would like to mention the very recent work in [4], in which the Lagrangian staggered scheme proposed in [5] is analyzed over a two-dimensional, uniform, periodic grid. The analysis in [4] is limited to the case of the implicit mid-point algorithm and the scheme corresponding to only one predictor and one corrector passes, for the case of a purely acoustic system, with no viscosity. This work is instead focussed on exploring the peculiar behavior of the even and odd iterations of the predictor/multi-corrector, including the effects of viscosity, and is in agreement with the specific cases discussed in [4].

The analysis of stability applies to the linearized, small-perturbation form of the Lagrangian hydrodynamics equations. In this case, due to the smallness of the displacements, the small-strain approximation is applied (i.e., the gradients in the

☆ This research was partially funded by the DOE NNSA Advanced Scientific Computing Program and the Computer Science Research Institute at Sandia National Laboratories. Sandia is a multiprogram laboratory operated by Sandia Corporation, a Lockheed Martin Company, for the United States Department of Energy under Contract DEAC04-94-AL85000.

* Corresponding author.
E-mail address: gscovaz@sandia.gov (G. Scovazzi).

0021-9991/$ - see front matter © 2009 Elsevier Inc. All rights reserved.
doi:10.1016/j.jcp.2009.06.042

current configuration of the material are approximated by the gradients in the original configuration). In addition, the values of thermodynamic variables are given by small perturbations superposed to constant reference values. The linearized approach pursued here is therefore a specific limit case of the more general nonlinear Lagrangian hydrodynamics equations. In this context, a proof of instability for the linearized case directly implies instability in the more general nonlinear case. With compelling numerical evidence, we show how the instabilities predicted in the linear case also arise in the more general nonlinear case, and that conditional stability limits derived in the linear case, when present, are also very reliable in the nonlinear case.

The rest of the exposition is organized as follows: Section 2 is devoted to presenting the equations of Lagrangian hydrodynamics, deriving an appropriate and representative linearization. In Section 3, a discrete system of equations is obtained in the case of one dimension and periodic boundary conditions. By means of the Discrete Fourier Transform, the von Neumann stability analysis is applied in Section 4 to the system of discrete equations. Section 5 is devoted to the analysis of the purely acoustic system of equations. In Section 6 the analysis is restricted to the highest wave numbers, with the purpose of deriving a simple stability bound for the time step in practical computations. In Section 7 the effect of viscosity on the stability of all discrete modes is also accounted for. A number of one-dimensional compressible flow computations are presented in Section 8, to confirm the theoretical findings also in the nonlinear case, for an ideal gas. A summary is presented in Section 9.

2. A simplified Lagrangian hydrodynamics system

In order to apply the von Neumann stability analysis to the system of equations of Lagrangian shock hydrodynamics, a linearization procedure is necessary. To this goal, we briefly summarize the system of Lagrangian equations for a compressible fluid in which heat fluxes, heat sources, and body forces are absent. Let Ω_0 and Ω be open sets in $\mathbb{R}^{n_d}$ (where n_d is the number of spatial dimensions). The *deformation*

$$\boldsymbol{\varphi} : \Omega_0 \to \Omega = \boldsymbol{\varphi}(\Omega_0), \tag{1}$$

$$\boldsymbol{X} \mapsto \boldsymbol{x} = \boldsymbol{\varphi}(\boldsymbol{X}, t) \quad \forall \boldsymbol{X} \in \Omega_0,\ t \geqslant 0, \tag{2}$$

maps the material coordinate $\boldsymbol{X}$ (sometimes referred to as the *material*, or *Lagrangian*, coordinate), representing the initial position of an infinitesimal material particle of the body, to $\boldsymbol{x}$, the position of that particle in the current configuration (see Fig. 1). Ω_0 is the domain occupied by the body in its initial configuration, with boundary Γ_0. $\boldsymbol{\varphi}$ maps Ω_0 to Ω, the domain occupied by the body in its current configuration. The *deformation gradient* and *deformation Jacobian determinant* can be defined as

$$\boldsymbol{F} = \nabla_{\boldsymbol{X}} \boldsymbol{\varphi}, \tag{3}$$

$$J = \det(\boldsymbol{F}), \tag{4}$$

where $\nabla_{\boldsymbol{X}}$ is the gradient in the original configuration. In the domain Ω, the equations for the displacement update and conservation of mass, momentum, and energy read:

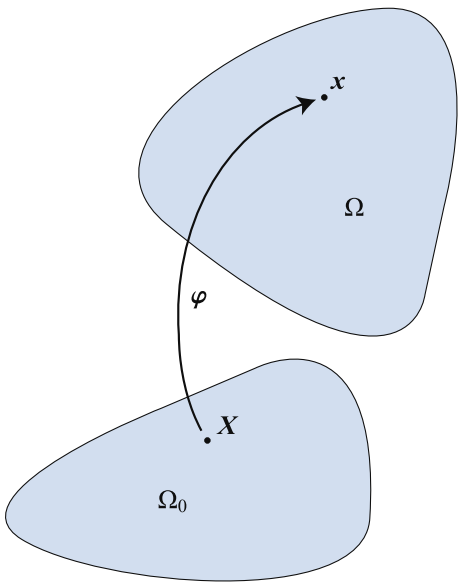

Fig. 1. Sketch of the Lagrangian map $\boldsymbol{\varphi}$.

$$\dot{\boldsymbol{u}} = \boldsymbol{v}, \tag{5}$$

$$\rho J = \rho_0, \tag{6}$$

$$0 = \rho \dot{\boldsymbol{v}} + \nabla_{\boldsymbol{x}} p - \nabla_{\boldsymbol{x}} \cdot (\rho \nu \nabla^s_{\boldsymbol{x}} \boldsymbol{v}), \tag{7}$$

$$0 = \rho \dot{\epsilon} + p \nabla_{\boldsymbol{x}} \cdot \boldsymbol{v} - \rho \nu \nabla^s_{\boldsymbol{x}} \boldsymbol{v} : \nabla^s_{\boldsymbol{x}} \boldsymbol{v}. \tag{8}$$

Here, $\nabla_{\boldsymbol{x}}$ and $\nabla_{\boldsymbol{x}} \cdot$ are the current configuration gradient and divergence operators, and $\dot{(\cdot)}$ indicates the material, or Lagrangian, time derivative. $\boldsymbol{u} = \boldsymbol{x} - \boldsymbol{X}$ is the displacement vector, ρ_0 is the reference (initial) density, ρ is the (current) density, $\boldsymbol{v}$ is the velocity, and p is the pressure, assumed to abide an equation of state of the type $p = \hat{p}(\rho, \epsilon)$, with ϵ the internal energy per unit mass.

Remark 1. We are considering the general case of a fluid with viscous stresses. The viscosity might be either physical or artificial (as in shock-capturing operators for Lagrangian transient algorithms).

2.1. Structure of the Lagrangian shock hydrodynamics flows

It is important at this point to further elaborate on the structure of the Lagrangian shock hydrodynamic systems, and obtain a set of equations amenable to the analysis of stability. To this end, recall that, if an equation of state of the type $\epsilon = \hat{\epsilon}(\rho, p)$ exists, then

$$d\epsilon = \left.\frac{\partial \epsilon}{\partial \rho}\right|_p d\rho + \left.\frac{\partial \epsilon}{\partial p}\right|_\rho dp. \tag{9}$$

Using the mass conservation equation in differential form

$$\dot{\rho} + \rho \nabla_{\boldsymbol{x}} \cdot \boldsymbol{v} = 0, \tag{10}$$

the energy Eq. (8) can be rearranged as:

$$\rho \nu \nabla^s_{\boldsymbol{x}} \boldsymbol{v} : \nabla^s_{\boldsymbol{x}} \boldsymbol{v} = \rho \dot{\epsilon} + p \nabla_{\boldsymbol{x}} \cdot \boldsymbol{v} = \rho \left.\frac{\partial \epsilon}{\partial \rho}\right|_p \dot{\rho} + \rho \left.\frac{\partial \epsilon}{\partial p}\right|_\rho \dot{p} + p \nabla_{\boldsymbol{x}} \cdot \boldsymbol{v} = \rho \left.\frac{\partial \epsilon}{\partial p}\right|_\rho \left(\dot{p} + \frac{\frac{p}{\rho} - \rho \left.\frac{\partial \epsilon}{\partial \rho}\right|_p}{\left.\frac{\partial \epsilon}{\partial p}\right|_\rho} \nabla_{\boldsymbol{x}} \cdot \boldsymbol{v} \right), \tag{11}$$

where, for a general compressible flow, $\rho \partial_p \epsilon|_\rho \neq 0$. It is possible to further manipulate the previous result using thermodynamic identities. First note that, by standard calculus derivations,

$$\left(\left.\frac{\partial \epsilon}{\partial p}\right|_\rho \right)^{-1} = \left.\frac{\partial p}{\partial \epsilon}\right|_\rho. \tag{12}$$

By Gibbs' identity (i.e., the combined first and second law of thermodynamics [6]) $d\epsilon - p/\rho^2 d\rho = \theta d\eta$ (θ being the temperature and η the entropy per unit mass),

$$\frac{p}{\rho} = \rho \left.\frac{\partial \epsilon}{\partial \rho}\right|_\eta. \tag{13}$$

Remark 2. Eq. (13) is intended to be an abstract thermodynamic relationship, and it is important to notice that we have *not* assumed that Lagrangian hydrodynamics flows are isentropic.

Combining (12) and (13) in the term multiplying the divergence in (11) yields

$$\frac{\frac{p}{\rho} - \rho \left.\frac{\partial \epsilon}{\partial \rho}\right|_p}{\left.\frac{\partial \epsilon}{\partial p}\right|_\rho} = \rho \left.\frac{\partial p}{\partial \epsilon}\right|_\rho \left(\left.\frac{\partial \epsilon}{\partial \rho}\right|_\eta - \left.\frac{\partial \epsilon}{\partial \rho}\right|_p \right) = \rho \left(\left.\frac{\partial p}{\partial \epsilon}\right|_\rho \left.\frac{\partial \epsilon}{\partial \rho}\right|_\eta - \left.\frac{\partial p}{\partial \epsilon}\right|_\rho \left.\frac{\partial \epsilon}{\partial \rho}\right|_p \right). \tag{14}$$

Eq. (14) can be further simplified recalling that a thermodynamic relation of the type $p = \hat{p}(\rho, \epsilon)$ yields

$$dp = \left.\frac{\partial p}{\partial \rho}\right|_\epsilon d\rho + \left.\frac{\partial p}{\partial \epsilon}\right|_\rho d\epsilon, \tag{15}$$

and, particularly,

$$0 = \left.\frac{\partial p}{\partial \rho}\right|_p = \left.\frac{\partial p}{\partial \rho}\right|_\epsilon + \left.\frac{\partial p}{\partial \epsilon}\right|_\rho \left.\frac{\partial \epsilon}{\partial \rho}\right|_p. \tag{16}$$

Substituting (16) into (14) yields

$$\frac{\frac{p}{\rho}-\rho\frac{\partial\epsilon}{\partial\rho}\Big|_p}{\frac{\partial\epsilon}{\partial p}\Big|_\rho}=\rho\left(\frac{\partial p}{\partial\epsilon}\Big|_\rho\frac{\partial\epsilon}{\partial\rho}\Big|_\eta-\frac{\partial p}{\partial\epsilon}\Big|_\rho\frac{\partial\epsilon}{\partial\rho}\Big|_p\right)=\rho\left(\frac{\partial p}{\partial\epsilon}\Big|_\rho\frac{\partial\epsilon}{\partial\rho}\Big|_\eta+\frac{\partial p}{\partial\rho}\Big|_\epsilon\right)=\rho\frac{\partial p}{\partial\rho}\Big|_\eta=\rho c_s^2, \tag{17}$$

where c_s is the isentropic speed of sound in the medium. Hence (11) reduces to

$$\rho\frac{\partial\epsilon}{\partial p}\Big|_\rho(\dot{p}+\rho c_s^2\nabla_{\boldsymbol{x}}\cdot\boldsymbol{v})=\rho\nu\nabla_{\boldsymbol{x}}^s\boldsymbol{v}:\nabla_{\boldsymbol{x}}^s\boldsymbol{v}. \tag{18}$$

Defining the Grüneisen parameter [14] as

$$\Gamma=\frac{1}{\rho\frac{\partial\epsilon}{\partial p}\Big|_\rho}=\frac{1}{\rho}\frac{\partial p}{\partial\epsilon}\Big|_\rho, \tag{19}$$

and recalling that $\Gamma\neq 0$ for a compressible fluid, Eq. (18) yields

$$\dot{p}+\rho c_s^2\nabla_{\boldsymbol{x}}\cdot\boldsymbol{v}=\Gamma(\rho\nu\nabla_{\boldsymbol{x}}^s\boldsymbol{v}:\nabla_{\boldsymbol{x}}^s\boldsymbol{v}). \tag{20}$$

Remark 3. For an ideal gas satisfying a γ-law equation of state, it is easy to derive $\Gamma=\gamma-1=$ constant.

The momentum and energy equations can be combined into the mixed, first-order system form of a nonlinear dissipative wave equation in $\boldsymbol{v}$ and p:

$$\rho\dot{\boldsymbol{v}}+\nabla_{\boldsymbol{x}}p=\nabla_{\boldsymbol{x}}\cdot(\rho\nu\nabla_{\boldsymbol{x}}^s\boldsymbol{v}), \tag{21}$$
$$\dot{p}+\rho c_s^2\nabla_{\boldsymbol{x}}\cdot\boldsymbol{v}=\Gamma(\rho\nu\nabla_{\boldsymbol{x}}^s\boldsymbol{v}:\nabla_{\boldsymbol{x}}^s\boldsymbol{v}). \tag{22}$$

2.2. Linearization of the equations

Assume the solution is small with regard to the kinematic variables (velocity, displacement, acceleration), that is

$$\boldsymbol{v}=\boldsymbol{v}'\ll 1, \tag{23}$$
$$\boldsymbol{u}=\boldsymbol{u}'\ll 1, \tag{24}$$

and that the solution for the thermodynamic variables (density, pressure, internal energy) is given by a small perturbation of constant reference fields, namely:

$$\rho=\bar{\rho}+\rho',\quad \bar{\rho}=\text{const.},\quad \rho'\ll 1 \tag{25}$$
$$p=\bar{p}+p',\quad \bar{p}=\text{const.},\quad p'\ll 1 \tag{26}$$
$$c_s=\bar{c}_s+c_s',\quad \bar{c}_s=\text{const.},\quad c_s'\ll 1 \tag{27}$$

Hence, by neglecting quadratic and higher-order terms, the linearized version of (21) and (22) is given by:

$$\bar{\rho}\dot{\boldsymbol{v}}'+\nabla_{\boldsymbol{X}}p'=\bar{\rho}\bar{\nu}\nabla_{\boldsymbol{X}}\cdot(\nabla_{\boldsymbol{X}}^s\boldsymbol{v}'), \tag{28}$$
$$\dot{p}'+\bar{\rho}\bar{c}_s^2\nabla_{\boldsymbol{X}}\cdot\boldsymbol{v}'=0. \tag{29}$$

Remark 4. Note that the viscous term in the energy equation is negligible with respect to the other terms, as it is quadratic in the velocity.

Remark 5. Linearization implies the small-strain approximation, which allows for the simplification $\nabla_{\boldsymbol{x}}\approx\nabla_{\boldsymbol{X}}$ (the motion of the mesh is neglected when computing gradients).

Remark 6. If the same linearization procedures are applied to the displacement Eq. (5) and the differential form of the mass conservation Eq. (10), the result is

$$\dot{\boldsymbol{u}}'=\boldsymbol{v}', \tag{30}$$
$$\dot{\rho}'+\bar{\rho}\nabla_{\boldsymbol{X}}\cdot\boldsymbol{v}'=0. \tag{31}$$

Observe that the linearized mass and displacement equations *decouple* from the linearized momentum and energy equations. For this reason, we will only consider the system of linearized momentum and energy equations in the analysis that follows.

Remark 7. For the sake of simplicity, we will drop the primes and bars from Eqs. (28) and (29).

In order to achieve insightful results, we will consider a simple one-dimensional flow with periodic boundary conditions. The reader will appreciate that the subsequent derivations are quite involved, and that these assumptions are essential to obtain meaningful results.

3. One-dimensional linearized variational formulation

We consider a weak formulation of the one-dimensional linearized equations of Lagrangian shock hydrodynamics, augmented by a shock capturing artificial viscosity operator [18]. Namely, denoting by $\mathbb{T}$ the unit periodic torus along the real line $\mathbb{R}$, we have, for every piece-wise linear (continuous) shape function ψ and every piece-wise constant (discontinuous) shape function ϕ,

$$0 = \int_{\mathbb{T}} \psi \dot{V} - \int_{\mathbb{T}} \psi_{,X} P + \int_{\mathbb{T}} \psi_{,X} \nu V_{,X}, \tag{32}$$

$$0 = \int_{\mathbb{T}} \phi \dot{P} + \int_{\mathbb{T}} \phi c_s^2 V_{,X}, \tag{33}$$

where, for the sake of simplicity, we have denoted $V = \rho v$ (recall $\rho = \text{const.}$) and $P = p$. Using the same predictor/multi-corrector strategy adopted in [19], the discretization in time of (32) and (33) yields:

$$0 = \int_{\mathbb{T}} \psi (V_{n+1}^{(i+1)} - V_n) - \Delta t \int_{\mathbb{T}} \psi_{,X} P_{n+1/2}^{(i)} + \Delta t \int_{\mathbb{T}} \psi_{,X} \nu (V_{,X})_{n+1/2}^{(i)}, \tag{34}$$

$$0 = \int_{\mathbb{T}} \phi (P_{n+1}^{(i+1)} - P_n) + \Delta t \int_{\mathbb{T}} \phi c_s^2 (V_{,X})_{n+1/2}^{(i+1)}, \tag{35}$$

where $(\cdot)^{(i)}$ and $(\cdot)^{(i+1)}$ are used to denote quantities computed with the predictor/corrector iterates (i) and $(i+1)$, respectively, and the subscripts $n, n+1$, and $n+1/2$ are used to indicate quantities at time $t_n, t_n + 1$, and $t_{n+1/2} = (t_n + t_{n+1})/2$.

Remark 8. Observe that the latest available velocity iterate is used in the computation of the second term of (35), as in [2,5,17,18], with the purpose of conserving total energy in the nonlinear setting. This time discretization is adopted to keep the analysis as close as possible to the algorithm effectively used in the computations in [2,5,17,18], and we refer to this method as the *conservative* time integrator.

Assume a uniform, equispaced subdivision of the torus $\mathbb{T}$ into finite elements of measure h. The velocities are approximated by piece-wise linear functions with degrees-of-freedom collocated at the nodes of the discretization, while the pressures are approximated by piece-wise constants, with degrees-of-freedom collocated at the barycenters of the elements (staggered spatial discretization). In addition to the previous assumptions, mass lumping is adopted in the momentum equation, yielding the following finite difference equations:

$$\begin{aligned} 0 = {} & V_{j,n+1}^{(i+1)} - V_{j,n} + \frac{\sigma}{2c_s}\left(P_{j+1/2,n+1}^{(i)} + P_{j+1/2,n} - P_{j-1/2,n+1}^{(i)} - P_{j-1/2,n}\right) \\ & + \frac{\kappa}{2}\left(-V_{j+1,n+1}^{(i)} - V_{j+1,n} + 2V_{j,n+1}^{(i)} + 2V_{j,n} - V_{j-1,n+1}^{(i)} - V_{j-1,n}\right), \end{aligned} \tag{36}$$

$$0 = P_{j+1/2,n+1}^{(i+1)} - P_{j+1/2,n} + \frac{c_s \sigma}{2}(V_{j+1,n+1}^{(i+1)} + V_{j+1,n} - V_{j-1,n+1}^{(i+1)} - V_{j-1,n}), \tag{37}$$

where $\sigma = \frac{c_s \Delta t}{h}$ is the acoustic Courant number, $\kappa = \frac{\nu \Delta t}{h^2}$, and j is the node index.

Remark 9. In the simple one-dimensional, periodic case, Eqs. (36) and (37) exactly coincide with the one-dimensional version of the finite difference schemes detailed in [2,5].

4. von Neumann stability analysis

As customary in the von Neumann stability analysis (see [15,20] for details), because the boundary conditions are periodic, the solution degrees-of-freedom can be expanded as a finite, linear combination of complex exponentials with complex coefficients. This eventually amounts to applying a Discrete Fourier Transform (DFT) operator to the discrete Eqs. (36) and (37). In particular, we have:

$$V_{j,n}^{(i)} = \sum_{k=-N/2+1}^{N/2} \widehat{V}_{k,n}^{(i)} e^{\mathrm{i}\beta_k j}, \tag{38}$$

$$P_{j+1/2,n}^{(i)} = \sum_{k=-N/2+1}^{N/2} \widehat{P}_{k,n}^{(i)} e^{\mathrm{i}\beta_k (j+1/2)}, \tag{39}$$

where $\mathrm{i} = \sqrt{-1}$, and $\widehat{V}_{k,n}^{(i)}$ is the Fourier coefficient associated with the kth harmonic, time step n and iterate (i). Note that N is the number of elements (a multiple of 2), and $\beta_k = \frac{2\pi h k}{|\mathbb{T}|} = \frac{2\pi k}{N}$ is an angularly scaled version of the integer wave number k

(with $|\mathbb{T}| = \mathrm{meas}(\mathbb{T}) = Nh = 1$ the measure of the torus). Complex exponentials associated to different wave numbers satisfy a discrete orthogonality property:

$$\sum_{m=-N/2}^{N/2-1} e^{i\beta_k m} e^{i\beta_q m} = \delta_{kq}, \quad \text{for } -N/2 \leqslant k, q \leqslant N/2, \tag{40}$$

with δ_{kq} the Kronecker delta tensor ($\delta_{kq} = 1$ if $k = q$, and $\delta_{kq} = 0$ if $k \neq q$). Substitute (38) and (39) into (36) and (37) multiplied by $e^{i\beta_{k_1} j}$ and $e^{i\beta_{k_2}(j+1/2)}$, respectively, and sum over j. We multiply (37) by $e^{i\beta_{k_2}(j+1/2)}$ instead of $e^{i\beta_{k_2} j}$, in order to simplify the algebra, as the pressure variable is staggered in space with respect to the momentum equation.

Due to the orthogonality property (40), and the linearity of the system of Eqs. (36) and (37), it is easy to verify that the previous steps lead to N pairs of equations, coupling the dynamics of the kth pressure and velocity modes, with $-N/2 + 1 \leqslant k \leqslant N/2$. Namely:

$$(\boldsymbol{I} + \boldsymbol{A}_0)\widehat{\boldsymbol{Z}}^{(i+1)}_{k,n+1} = \boldsymbol{A}_1 \widehat{\boldsymbol{Z}}^{(i)}_{k,n+1} + (\boldsymbol{I} + \boldsymbol{A}_2)\widehat{\boldsymbol{Z}}_{k,n}, \tag{41}$$

where

$$\widehat{\boldsymbol{Z}}^{(i)}_{k,n} = \begin{Bmatrix} \widehat{V}^{(i)}_{k,n} \\ \widehat{P}^{(i)}_{k,n} \end{Bmatrix} \tag{42}$$

is the kth velocity/pressure modal pair, relative to the nth time step and the ith iterate, and

$$\boldsymbol{I} = \begin{bmatrix} 1 & 0 \\ 0 & 1 \end{bmatrix}, \tag{43}$$

$$\boldsymbol{A}_0 = \begin{bmatrix} 0 & 0 \\ \mathrm{i}\frac{c_s}{2}\sigma \sin\left(\frac{\beta_k}{2}\right) & 0 \end{bmatrix}, \tag{44}$$

$$\boldsymbol{A}_1 = \begin{bmatrix} \kappa(\cos(\beta_k) - 1) & -\mathrm{i}\frac{1}{2c_s}\sigma \sin\left(\frac{\beta_k}{2}\right) \\ 0 & 0 \end{bmatrix}, \tag{45}$$

$$\boldsymbol{A}_2 = \begin{bmatrix} \kappa(\cos(\beta_k) - 1) & -\mathrm{i}\frac{1}{2c_s}\sigma \sin\left(\frac{\beta_k}{2}\right) \\ -\mathrm{i}\frac{c_s}{2}\sigma \sin\left(\frac{\beta_k}{2}\right) & 0 \end{bmatrix}. \tag{46}$$

It is also very important to observe that because the degrees-of-freedom "signal" has real values, the discrete Fourier coefficients must satisfy the complex conjugacy property

$$\widehat{\boldsymbol{Z}}^{(i)}_{-k,n} = (\widehat{\boldsymbol{Z}}^{(i)}_{k,n})^*, \quad \text{for } 0 \leqslant k \leqslant N/2 - 1, \tag{47}$$

where $\widehat{\boldsymbol{W}}^*$ indicates the complex conjugate of $\widehat{\boldsymbol{W}}$ (componentwise). For the same reason, the following condition on the often called "odd ball" mode holds:

$$\widehat{\boldsymbol{Z}}^{(i)}_{N/2,n} = \boldsymbol{0}. \tag{48}$$

Because complex conjugates have the same absolute value and opposite phase, it is sufficient to limit the study of the amplification factors for the modes of the discrete system to the range $0 \leqslant k < N/2$, that is, $0 \leqslant \beta_k < \pi$. In the discussion that follows, it will also be important to consider a variation of the time-integration algorithm, in which the velocity iterate $V^{(i+1)}$ in (37) is replaced by the previous iterate $V^{(i)}$. This method will be referred to as the *lagged* approach. In this case, Eq. (37) becomes

$$0 = P^{(i+1)}_{j+1/2,n+1} - P_{j+1/2,n} + \frac{c_s\sigma}{2}\left(V^{(i)}_{j+1,n+1} + V_{j+1,n} - V^{(i)}_{j-1,n+1} - V_{j-1,n}\right), \tag{49}$$

and, consequently, $\boldsymbol{A}_0$ and $\boldsymbol{A}_1$ need to be modified as:

$$\boldsymbol{A}_0 = \boldsymbol{0}, \tag{50}$$

$$\boldsymbol{A}_1 = \boldsymbol{A}_2. \tag{51}$$

This approach yields a more straightforward time integrator for the linearized equations, which does not extend, however, to a conservative scheme in the nonlinear case.

The vector Eq. (41) is a recurrence relationship between the predictor/multi-corrector iterates of the proposed time-integration approach. Set

$$\boldsymbol{B}_0 = (\boldsymbol{I} + \boldsymbol{A}_0)^{-1}(\boldsymbol{I} + \boldsymbol{A}_2), \tag{52}$$

$$\boldsymbol{B}_1 = (\boldsymbol{I} + \boldsymbol{A}_0)^{-1}\boldsymbol{A}_1, \tag{53}$$

and recall that the first guess for the new iterate at time t_{n+1} is the solution at time t_n, namely $\widehat{\boldsymbol{Z}}^{(0)}_{k,n+1} = \widehat{\boldsymbol{Z}}_{k,n}$. Then, we can derive explicit recurrence formulas for the computation of $\widehat{\boldsymbol{Z}}^{(i+1)}_{k,n+1}$ in terms of $\widehat{\boldsymbol{Z}}_{k,n}$:

$$\widehat{\boldsymbol{Z}}^{(1)}_{k,n+1} = \boldsymbol{B}_1\widehat{\boldsymbol{Z}}^{(0)}_{k,n+1} + \boldsymbol{B}_0\widehat{\boldsymbol{Z}}_{k,n} = (\boldsymbol{B}_0 + \boldsymbol{B}_1)\widehat{\boldsymbol{Z}}_{k,n} = \boldsymbol{G}^{(1)}\widehat{\boldsymbol{Z}}_{k,n}, \tag{54}$$

$$\widehat{\boldsymbol{Z}}^{(2)}_{k,n+1} = \boldsymbol{B}_1\widehat{\boldsymbol{Z}}^{(1)}_{k,n+1} + \boldsymbol{B}_0\widehat{\boldsymbol{Z}}_{k,n} = (\boldsymbol{B}_1\boldsymbol{G}^{(1)} + \boldsymbol{B}_0)\widehat{\boldsymbol{Z}}_{k,n} = \boldsymbol{G}^{(2)}\widehat{\boldsymbol{Z}}_{k,n},, \tag{55}$$

$$\widehat{\boldsymbol{Z}}^{(3)}_{k,n+1} = \boldsymbol{B}_1\widehat{\boldsymbol{Z}}^{(2)}_{k,n+1} + \boldsymbol{B}_0\widehat{\boldsymbol{Z}}_{k,n} = (\boldsymbol{B}_1\boldsymbol{G}^{(2)} + \boldsymbol{B}_0)\widehat{\boldsymbol{Z}}_{k,n} = \boldsymbol{G}^{(3)}\widehat{\boldsymbol{Z}}_{k,n}, \tag{56}$$

$$\widehat{\boldsymbol{Z}}^{(4)}_{k,n+1} = \boldsymbol{B}_1\widehat{\boldsymbol{Z}}^{(3)}_{k,n+1} + \boldsymbol{B}_0\widehat{\boldsymbol{Z}}_{k,n} = (\boldsymbol{B}_1\boldsymbol{G}^{(3)} + \boldsymbol{B}_0)\widehat{\boldsymbol{Z}}_{k,n} = \boldsymbol{G}^{(4)}\widehat{\boldsymbol{Z}}_{k,n},, \tag{57}$$

$$\widehat{\boldsymbol{Z}}^{(5)}_{k,n+1} = \cdots \tag{58}$$

In the limit for an infinite number of iterations, we obtain the amplification matrix for the original implicit mid-point algorithm from which the predictor/corrector time integrator is derived:

$$(\boldsymbol{I} + \boldsymbol{A}_0)\widehat{\boldsymbol{Z}}^{(\infty)}_{k,n+1} = \boldsymbol{A}_1\widehat{\boldsymbol{Z}}^{(\infty)}_{k,n+1} + (\boldsymbol{I} + \boldsymbol{A}_2)\widehat{\boldsymbol{Z}}_{k,n}, \tag{59}$$

that is, removing the superscript (∞) from $\widehat{\boldsymbol{Z}}^{(\infty)}_{k,n+1}$, and rearranging terms,

$$\widehat{\boldsymbol{Z}}_{k,n+1} = (\boldsymbol{I} + \boldsymbol{A}_0 - \boldsymbol{A}_1)^{-1}(\boldsymbol{I} + \boldsymbol{A}_2)\,\widehat{\boldsymbol{Z}}_{k,n} = \boldsymbol{G}^{(\infty)}\widehat{\boldsymbol{Z}}_{k,n}. \tag{60}$$

Remark 10. The predictor/multi-corrector method can therefore be interpreted as a fixed-point iterative process, converging to the solution of the implicit method (60). In particular, the conservative scheme has the nature of a Gauss–Seidel iteration, as the matrix $\boldsymbol{I} + \boldsymbol{A}_0$ is lower diagonal, while the lagged scheme resembles a Jacobi iteration, since in this case $\boldsymbol{A}_0 = \boldsymbol{0}$.

Remark 11. Convergence of the fixed-point iteration is ensured if $\|\boldsymbol{B}_1\| < 1$ (sufficient condition). It will be subsequently shown that this condition is equivalent to the temporal stability condition.

It is possible to evaluate the stability properties of the proposed predictor/multi-corrector algorithm, by evaluating how $\boldsymbol{G}^{(i)}$ evolves in time an initial condition. In particular, if

$$\|\boldsymbol{G}^{(i)}\| = \max_{\boldsymbol{s}\in\mathbb{R}^2\setminus\boldsymbol{0}} \frac{\|\boldsymbol{G}^{(i)}\boldsymbol{s}\|}{\|\boldsymbol{s}\|} \leqslant 1 \tag{61}$$

then stability of the numerical discretization is ensured. Defining the spectral radius as

$$\rho(\boldsymbol{G}^{(i)}) = \max\{|\lambda(\boldsymbol{G}^{(i)})|\} \leqslant \|\boldsymbol{G}^{(i)}\|, \tag{62}$$

where $\lambda(\boldsymbol{G}^{(i)})$ is a (generally complex) eigenvalue of $\boldsymbol{G}^{(i)}$, we can recast condition (61) as (see [9])

$$\rho(\boldsymbol{G}^{(i)}) < 1 \Rightarrow \text{stability}, \tag{63}$$

$$\rho(\boldsymbol{G}^{(i)}) > 1 \Rightarrow \text{instability}. \tag{64}$$

These conditions are consequence of a well-known theorem in matrix analysis:

Theorem 1. (cf. [11], p. 298) *Let $\boldsymbol{A} \in \mathbb{C}^{m\times m}$, where $\mathbb{C}$ is the complex field. Then:* $\lim_{n\to\infty}\boldsymbol{A}^n = \boldsymbol{0}$ *if and only if* $\rho(\boldsymbol{A}) < 1$.

Hence, if $\rho(\boldsymbol{G}^{(i)}) < 1$, Theorem 1 directly implies stability. If $\rho(\boldsymbol{G}^{(i)}) > 1$, one can consider, as initial condition vector $\widehat{\boldsymbol{Z}}_0$, the eigenvector relative to an eigenvalue λ_0 with $|\lambda_0| > 1$. Using the properties of vector norms, it is easy to see that $\lim_{n\to\infty}\|\widehat{\boldsymbol{Z}}_n\| = \lim_{n\to\infty}\|(\boldsymbol{G}^{(i)})^n\widehat{\boldsymbol{Z}}_0\| = \lim_{n\to\infty}|\lambda_0|^n\|\widehat{\boldsymbol{Z}}_0\| = \infty$, and we have instability. The case that our analysis covers less precisely is the case when $\rho(\boldsymbol{G}^{(i)}) = 1$. Recalling that (see [11], p. 299)

$$\rho(\boldsymbol{G}^{(i)}) = \lim_{n\to\infty}\|(\boldsymbol{G}^{(i)})^n\|^{1/n}, \tag{65}$$

it is easy to realize that the case $\rho(\boldsymbol{G}^{(i)}) = 1$ admits linear growth in the solution (i.e., $\|(\boldsymbol{G}^{(i)})^n\| = O(n)$). However, the analysis that follows (see, e.g., Fig. 2) shows that $\rho(\boldsymbol{G}^{(i)}) = 1$ occurs in three special cases:

1. $\sigma = 0 \Longleftrightarrow \Delta t = 0$, a trivial case corresponding of no time evolution.
2. $\beta_k = 0$, corresponding to the evolution in time of a constant mode. In this case, it is not necessary to resort to the von Neumann analysis, to prove that the entire class of algorithms under consideration *stably* preserves constant solutions in time.
3. The time-step stability limit, as a limit case of the condition $\rho(\boldsymbol{G}^{(i)}) < 1$. This case is not so important in practical (nonlinear) computations, since it is usually not safe to run computations exactly at the stability limit.

Note also that a complex eigenvalue of $\boldsymbol{G}^{(i)}$ can be expressed as:

$$\lambda(\boldsymbol{G}^{(i)}) = |\lambda(\boldsymbol{G}^{(i)})|e^{i\bar{\omega}\Delta t}, \tag{66}$$

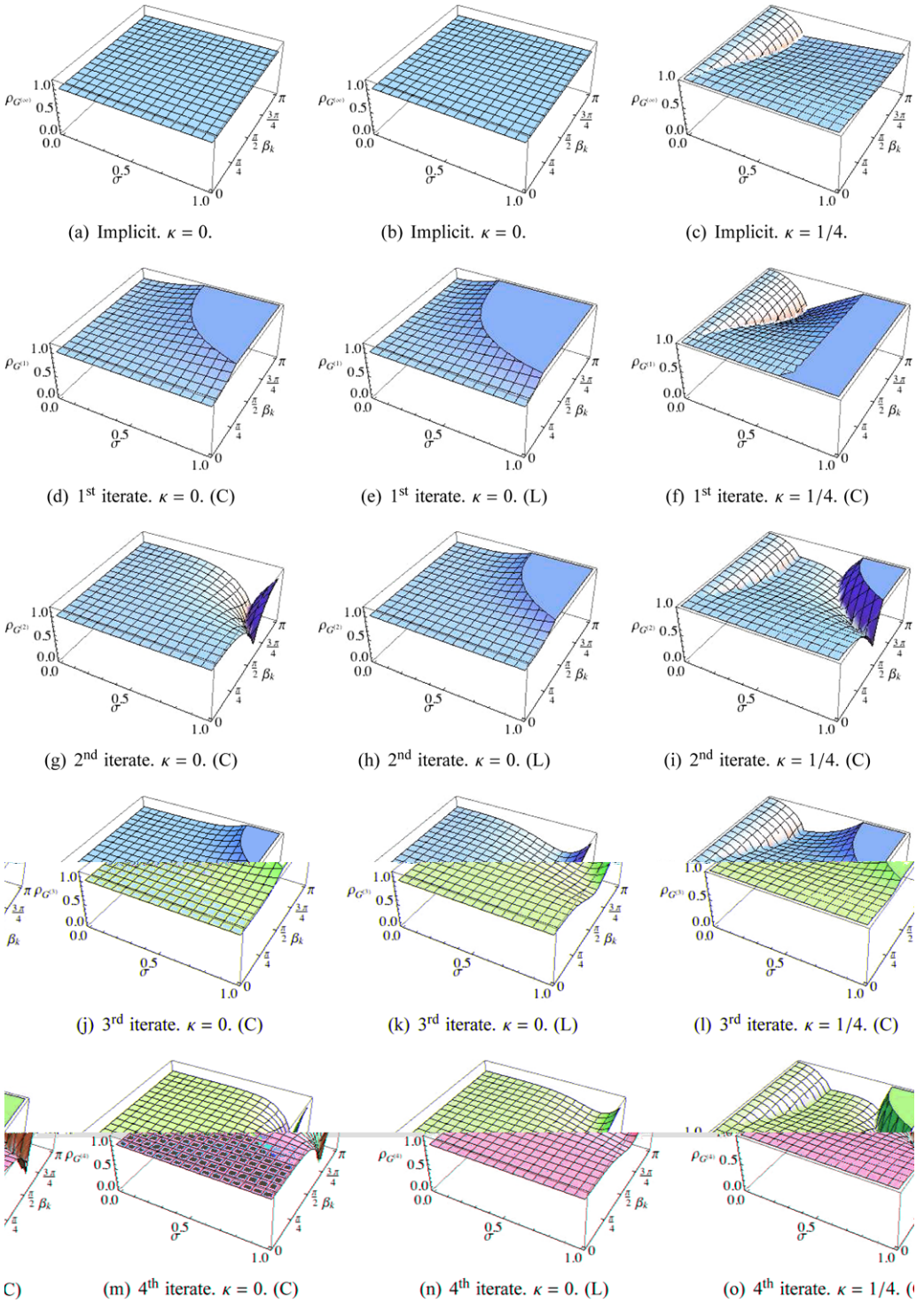

Fig. 2. Elevation plots of the spectral radii $\rho_{\mathbf{G}^{(i)}}(\sigma, \beta_k)$ for $\kappa = 0, \kappa = 1/4$, and various iterates of the predictor/multi-corrector algorithm. In the top row, the implicit mid-point time integrator detailed in (60). In the subsequent rows, in ascending order, the iterates from one to four. Note that in Fig. 2(a), (b), (d), (e), (g), (h), (j), (k), (m), and (n) the vertical range is [0,1.2], while in Fig. 2(c), (f), (i), (l), and (o) the vertical range is [0,1]. Also note that Fig. 2(a) and (b) are identical.

where $\bar{\omega}\Delta t = \arg(\lambda(\mathbf{G}^{(i)}))$, and $\bar{\omega} \in \mathbb{R}$ is the phase. This decomposition will be important for the study of the dispersion properties of the proposed time-integration approach. An alternative expression for (66) is

$$\lambda(\mathbf{G}^{(i)}) = e^{(-\bar{\xi}+i\bar{\omega})\Delta t}, \tag{67}$$

where

$$|\lambda(\boldsymbol{G}^{(i)})| = e^{-\bar{\xi}\Delta t} \quad \text{or} \quad \bar{\xi} = -\frac{\log(|\lambda(\boldsymbol{G}^{(i)})|)}{\Delta t}. \tag{68}$$

By performing a Taylor expansion of $\bar{\xi}$ and $\bar{\omega}$ in the limit of vanishing time step Δt and mesh size h, it is possible to recover the truncation error and the formal order of accuracy of the various iterates of the method.

Due to the complexity of the algebra involved, we are not including the calculations and explicit expressions of the eigenvalues of the $\boldsymbol{G}^{(i)}$ matrices in the general case. We will present the fundamental results by appropriate plots in Sections 5 and 7. All algebraic symbolic manipulations were performed using the MATHEMATICA®™ software [1,22] .

5. The case of vanishing viscosity

In shock hydrodynamics computations, the artificial viscosity is usually present only in shock layers, and absent in expansion regions. Therefore, it is very important to study the proposed time integrator in the limit of a vanishing viscosity, as most of the flow domain is subject to this condition.

5.1. Amplification factor

Fig. 2 shows the spectral radii of the matrices $\boldsymbol{G}^{(i)}$ for $i = 1, 2, 3, 4$ and $i \to \infty$ (implicit limit), for the conservative and lagged algorithms in the case $\kappa = 0$, and also for the conservative algorithm when $\kappa = 1/4$. For the time being, we focus on the plots relative to $\kappa = 0$.

First, note that the implicit algorithm detailed in (60) is neutrally stable (Fig. 2(a) and (b)), as the spectral radius of the corresponding amplification matrix is equal to unity over the entire plane $[\sigma, \beta]$. The first and third iterates of the conservative algorithm (C) are *unconditionally unstable*, while the second and fourth iterates are conditionally stable, as shown in Fig. 2(g) and (m). This phenomenon, somewhat surprising, can be explained by realizing that the spectral radii for the predictor/multi-corrrector scheme exhibit a *non-monotonic* convergence to unity as $(i) \to \infty$. Observe that the situation for the lagged algorithm is somewhat different, since the first two iterates are unconditionally unstable (Fig. 2(e) and (h)), but the subsequent third and fourth iterates regain conditional stability in the range $\sigma \in [0, 1]$ (Fig. 2(k) and (n)). This fact can easily be observed in the contour plots of the spectral radii presented in Fig. 3, and perhaps even more clearly in the sections at various values of σ presented in Fig. 4.

Also note in Fig. 4(d) that the second iterate, indicated by a red[1] line, shows the insurgence of a bifurcation (a kink in the red curve, near $\beta_k = 3\pi/4$). Past the bifurcation point, the eigenvalues of the amplification matrix cease to be complex conjugate and become real, as also evident in Fig. 7(d), by the absence of a phase in the eigenvalues. This is not a desirable property in wave propagation problems, where one would expect the discretized equations to behave as a system of harmonic oscillators. Past the bifurcation point, the discrete solutions become real exponentials in time, and cause an incorrect representation of the structure of the original system of partial differential equations. The lagged algorithm does not show this behavior.

5.2. Dispersion error

When no viscosity is present, it is very insightful to evaluate the extent of the dispersion error in computations. This can be done by observing that the classical dispersion relationship for a linear wave is given by $\omega = 2\pi k c_s/|\mathbb{T}|$. Recalling that $\mathbb{T} = hN$, it is easy to derive that

$$\omega \Delta t = \sigma \beta_k. \tag{69}$$

A typical measure of the dispersion error is given by the ratio

$$\frac{\bar{\omega}}{\omega} = \frac{\arg(\lambda(\sigma, \beta_k))}{\sigma \beta_k}. \tag{70}$$

Fig. 5 shows elevation plots of the ratio $\bar{\omega}/\omega$. It is noticeable in Fig. 5(e) and (i) that bifurcation takes place for values of $[\sigma, \beta_k]$ in the neighborhood of $[1, \pi]$, for the second and fourth iterate of the conservative algorithm, respectively. As already mentioned, this behavior is not present for the lagged scheme.

Contour plots of the dispersion ratio are presented in Fig. 6. The black thick lines indicate the loci where the dispersion ratio equals unity, that is, optimal behavior (no phase error).

Comparing the various results in Fig. 7, notice the good behavior of the conservative approach in retaining the dispersion properties of the corresponding implicit method, at least until a bifurcation arises for the second iterate (see Fig. 7(a)–(d)).

[1] For interpretation of color in Fig. 4, the reader is referred to the web version of this article.

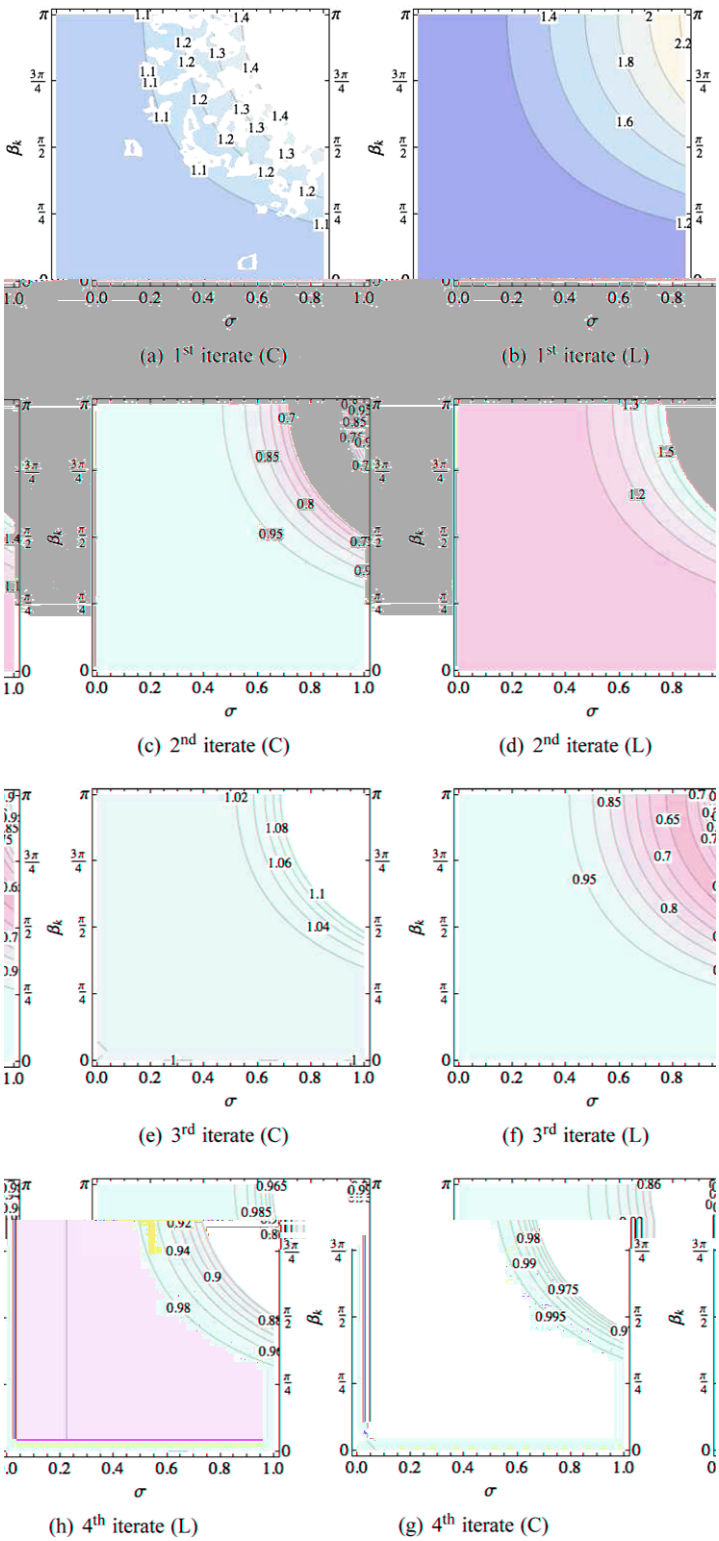

Fig. 3. Contour plots of the spectral radii of various iterates of the predictor/multi-corrector algorithm for $\kappa = 0$. Fig. 3(a), (c), (e), and (g): conservative scheme (C). Fig. 3(b), (d), (f), and (h): lagged scheme (L).

This is not the case for the lagged scheme, for which all the iterates have quite different phase characterization with respect to the implicit method (Fig. 7(e)–(h)).

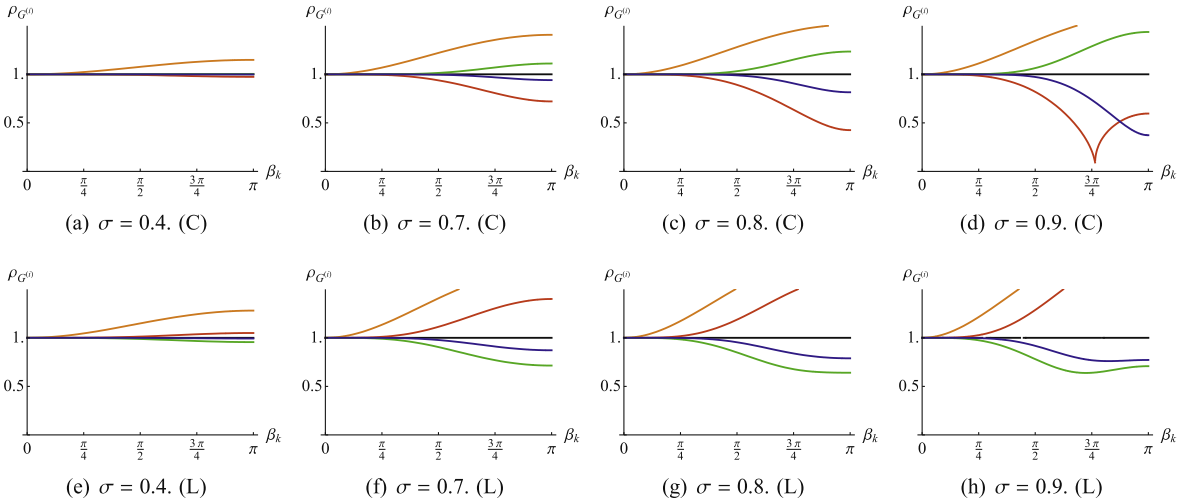

(a) $\sigma = 0.4$. (C) (b) $\sigma = 0.7$. (C) (c) $\sigma = 0.8$. (C) (d) $\sigma = 0.9$. (C)

(e) $\sigma = 0.4$. (L) (f) $\sigma = 0.7$. (L) (g) $\sigma = 0.8$. (L) (h) $\sigma = 0.9$. (L)

Fig. 4. Spectral radii for the predictor/multi-corrector algorithm in the case $\kappa = 0$, for various values of the acoustic Courant number σ. Fig. 4(a)–(d): Conservative scheme. Fig. 4(e)–(h): Lagged scheme. Black: Implicit time integrator. Orange, red, green and blue are used for the first, second, third, and fourth iterate, respectively. (For interpretation of the references to colour in this figure legend, the reader is referred to the web version of this article.)

5.3. Low wave number limit and truncation error

A Taylor expansion of the amplification factor ρ and dispersion ratio $\bar{\omega}/\omega$ in a right neighborhood of $\beta_k = 0$ can more clearly quantify the previous conclusions on the nature of the proposed conservative algorithm.

$$\rho(\boldsymbol{G}^{(1)}) = 1 + \frac{\sigma^2\beta_k^2}{4} + O(\beta_k^3), \quad \frac{\bar{\omega}(\boldsymbol{G}^{(1)})}{\omega} = 1 - \frac{4+11\sigma^2}{96}\beta_k^2 + O(\beta_k^4), \tag{71}$$

$$\rho(\boldsymbol{G}^{(2)}) = 1 - \frac{\sigma^4\beta_k^4}{16} + O(\beta_k^5), \quad \frac{\bar{\omega}(\boldsymbol{G}^{(2)})}{\omega} = 1 - \frac{2+\sigma^2}{24}\beta_k^2 + O(\beta_k^4), \tag{72}$$

$$\rho(\boldsymbol{G}^{(3)}) = 1 + \frac{\sigma^6\beta_k^6}{64} + O(\beta_k^7), \quad \frac{\bar{\omega}(\boldsymbol{G}^{(3)})}{\omega} = 1 - \frac{2+\sigma^2}{24}\beta_k^2 + O(\beta_k^4), \tag{73}$$

$$\rho(\boldsymbol{G}^{(4)}) = 1 - \frac{\sigma^8\beta_k^8}{256} + O(\beta_k^9), \quad \frac{\bar{\omega}(\boldsymbol{G}^{(4)})}{\omega} = 1 - \frac{2+\sigma^2}{24}\beta_k^2 + O(\beta_k^4). \tag{74}$$

Hence, it is clearly noticeable the fact that the low modes are amplified for odd iterates and damped for even iterates. The dispersion of low modes, instead, seems to maintain the same limit behavior as soon as the number of iterates is larger than one. Furthermore, a Taylor series expansion of $\bar{\xi}$ and $\bar{\omega}$ in powers of Δt and h allows to evaluate the order of convergence of the proposed method. We obtain:

$$\bar{\xi}(\boldsymbol{G}^{(1)}) = -\frac{1}{4}c_s^2\tilde{k}^2\Delta t + O(h^2\Delta t), \tag{75}$$

$$\bar{\omega}(\boldsymbol{G}^{(1)}) = \omega - \frac{1}{24}c_s h^2\tilde{k}^3 - \frac{11}{96}c_s^3\tilde{k}^3\Delta t^2 + O(\Delta t^2 h^2), \tag{76}$$

$$\bar{\xi}(\boldsymbol{G}^{(2)}) = \frac{1}{16}c_s^4\tilde{k}^4\Delta t^3 + O(h^2\Delta t^3), \tag{77}$$

$$\bar{\omega}(\boldsymbol{G}^{(2)}) = \omega - \frac{1}{24}c_s h^2\tilde{k}^3 - \frac{1}{12}c_s^3\tilde{k}^3\Delta t^2 + O(\Delta t^2 h^2), \tag{78}$$

$$\bar{\xi}(\boldsymbol{G}^{(3)}) = -\frac{1}{64}c_s^6\tilde{k}^6\Delta t^5 + O(h^2\Delta t^5), \tag{79}$$

$$\bar{\omega}(\boldsymbol{G}^{(3)}) = \omega - \frac{1}{24}c_s h^2\tilde{k}^3 - \frac{1}{12}c_s^3\tilde{k}^3\Delta t^2 + O(\Delta t^2 h^2), \tag{80}$$

$$\bar{\xi}(\boldsymbol{G}^{(4)}) = \frac{1}{256}c_s^8\tilde{k}^8\Delta t^7 + O(h^2\Delta t^7), \tag{81}$$

$$\bar{\omega}(\boldsymbol{G}^{(4)}) = \omega - \frac{1}{24}c_s h^2\tilde{k}^3 - \frac{1}{12}c_s^3\tilde{k}^3\Delta t^2 + O(\Delta t^2 h^2), \tag{82}$$

where $\tilde{\kappa} = 2\pi k/|\mathbb{T}|$, so that $\omega = \tilde{\kappa}c_s$. Consequently, the first, second, third and fourth iterates of the predictor/multi-corrector conservative method are first-, third-, fifth- and seventh-order accurate with respect to the dissipation error. All iterates are second-order accurate with respect to the dispersion error.

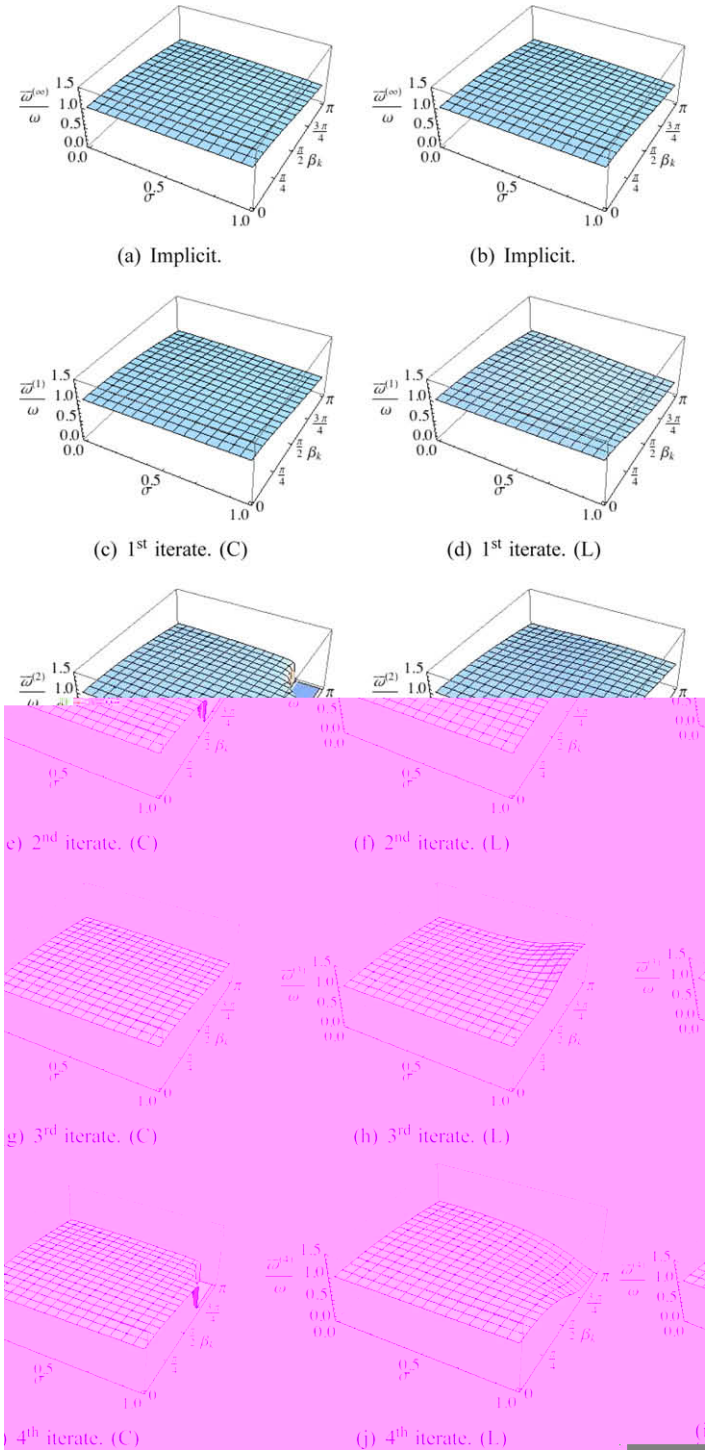

Fig. 5. Elevation plots of the dispersion ratio $\bar{\omega}/\omega$, for $\kappa = 0$, and various iterates of the predictor/multi-corrector algorithm. In the top row, the implicit mid-point time integrator detailed in (60). In the subsequent rows, in ascending order, the iterates from one to four. Fig. 5(a), (c), (e), (g), and (i) refer to the conservative algorithm (C), Fig. 5(b), (d), (f), (h), and (j) refer to the lagged algorithm (L). Also note that Fig. 5(a) and (b) are identical.

6. Stability of the highest wave numbers

Before proceeding with the case in which dissipation is present, it is important to develop a preliminary analysis of stability for the highest spatial wave numbers in the discrete equations. Stability of the highest modes in the computation is a necessary *but not sufficient* condition for overall stability. However, an understanding on the high wave number dynamics

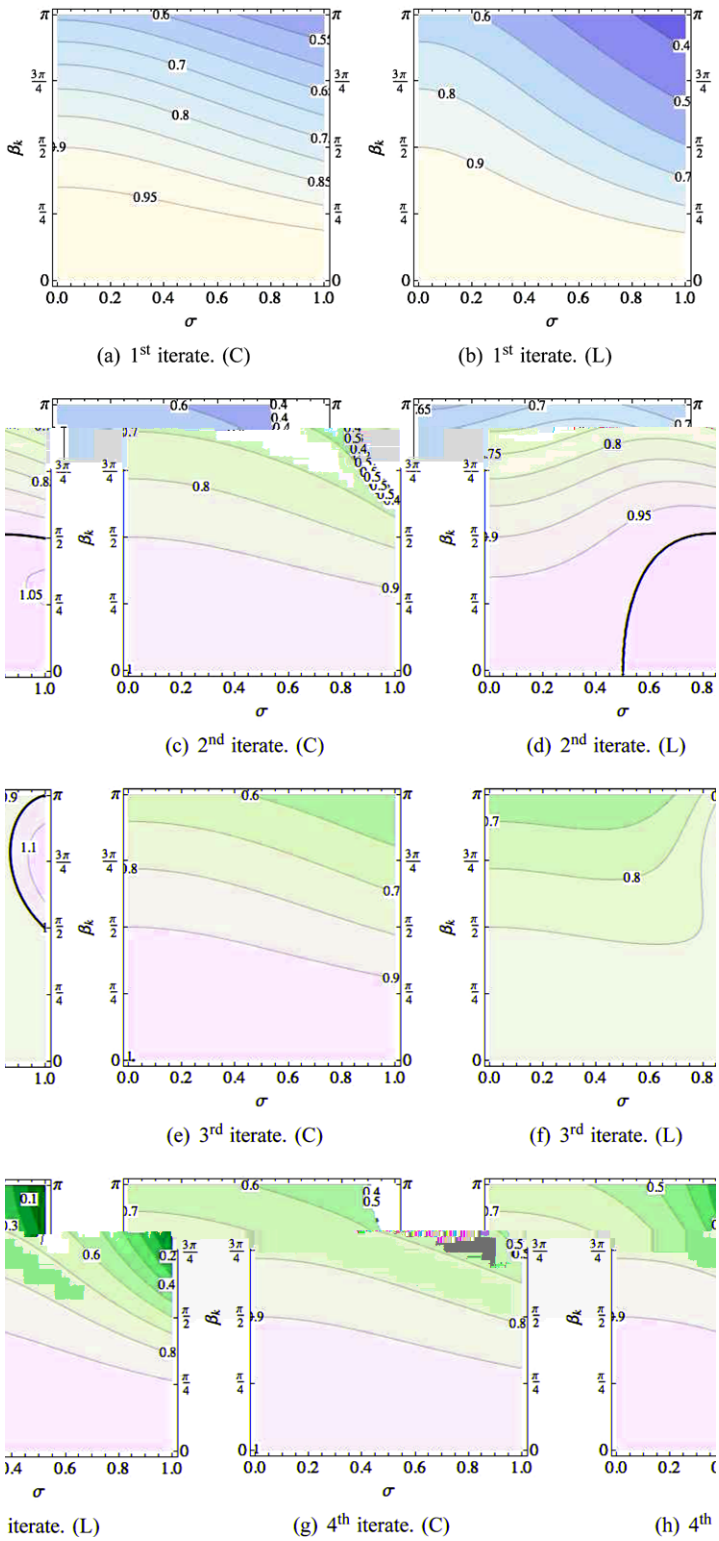

Fig. 6. Contour plots of the ratio $\bar{\omega}/\omega$, for $\kappa = 0$, and various iterates of the predictor/multi-corrector algorithm. Fig. 6(a), (c), (e), and (g): conservative scheme. Fig. 6(b), (d), (f), and (h): lagged scheme. The black continuous line indicates the locus $\bar{\omega}/\omega = 1$.

can shed light on the overall behavior of the algorithm, and, most importantly, provide stable time estimates of practical use in computations.

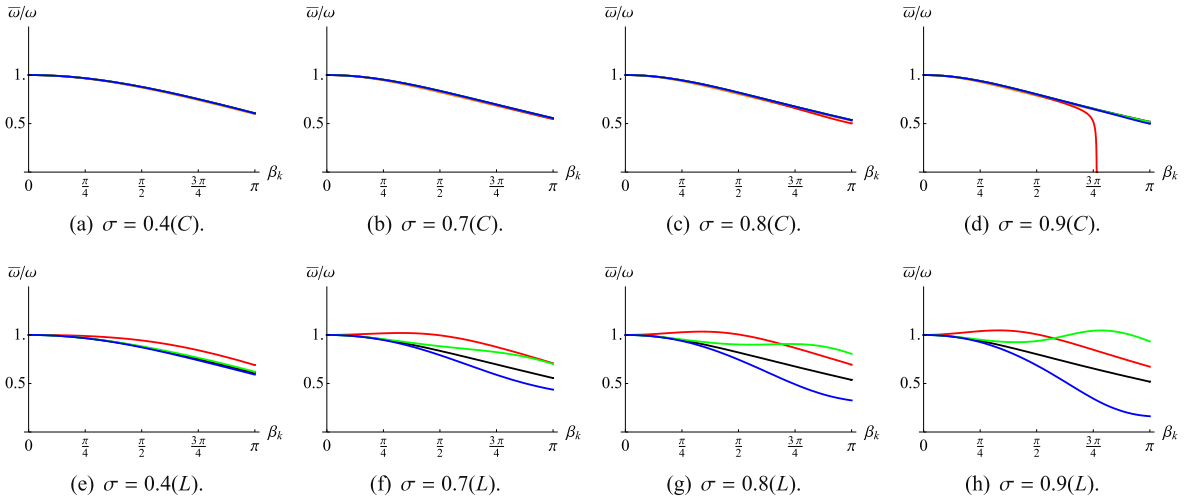

(a) $\sigma = 0.4(C)$. (b) $\sigma = 0.7(C)$. (c) $\sigma = 0.8(C)$. (d) $\sigma = 0.9(C)$.

(e) $\sigma = 0.4(L)$. (f) $\sigma = 0.7(L)$. (g) $\sigma = 0.8(L)$. (h) $\sigma = 0.9(L)$.

Fig. 7. Plot of the ratio $\bar{\omega}/\omega$, for $\kappa = 0$, for various values of the acoustic Courant number σ. Fig. 7(a)–(d): conservative scheme. Fig. 7(e)–(h): Lagged scheme. Color scheme is as follows. Black is used for the implicit version of the algorithm. Orange, red, green and blue are used for the first, second, third, and fourth iterate, respectively. (For interpretation of the references to colour in this figure legend, the reader is referred to the web version of this article.)

The amplification of the highest wave number is governed by the matrices $\boldsymbol{G}^{(i)}$, when β_k is set equal to π. In this case, a number of algebraic manipulations leads to the following expressions for the eigenvalues of the matrices $\boldsymbol{G}^{(i)}$'s:

$$\lambda_{1,2}^{(1)} = 1 - \sigma^2 - 2\kappa \tag{83}$$

$$\mp\sqrt{\sigma^4 + 4\sigma^2(-1+\kappa) + 4\kappa^2}, \tag{84}$$

$$\lambda_{1,2}^{(2)} = 1 - 2\sigma^2 + \sigma^4 - 2\kappa + 4\sigma^2\kappa + 4\kappa^2 \tag{85}$$

$$\mp\sqrt{-1 + 2\sigma^4 + 4\kappa - 8\kappa^2 + (1 + \sigma^4 - 2\kappa + 4\kappa^2 + \sigma^2(-2+4\kappa))^2}, \tag{86}$$

$$\lambda_{1,2}^{(3)} = \cdots, \tag{87}$$

where we have omitted the derivations for the third and higher iterates, since the algebraic expressions become very complex and tedious to manipulate. Let us consider the second iterate, that is the first iterate for which second-order accuracy is achieved, and analyze the stability condition $-1 \leqslant \lambda_{1,2}^{(2)} \leqslant 1$. Only the right bound is meaningful for stability. Setting $\lambda_{1,2}^{(2)} = 1$ yields a polynomial equation, with roots $\sigma = 0, \sigma = -\sqrt{1-2\kappa}$, and $\sigma = \sqrt{1-2\kappa}$. Only the last root is useful in defining a stability limit, which, taking squares, reads

$$\sigma^2 + 2\kappa - 1 \leqslant 0 \quad \text{or} \quad c_s^2\Delta t^2 + 2v\Delta t - h^2 \leqslant 0. \tag{88}$$

The same condition is derived in the case of four iterations of the predictor/multi-corrector algorithm, with much more complex algebraic manipulations. Solving the quadratic equation associated with (88) yields the bounds

$$\frac{-v - \sqrt{v^2 + c_s^2h^2}}{c_s^2} \leqslant \Delta t \leqslant \frac{-v + \sqrt{v^2 + c_s^2h^2}}{c_s^2}. \tag{89}$$

The left bound is always verified, while the right gives the stability limit. Multiplying and dividing the entire inequality by $v + \sqrt{v^2 + c_s^2h^2}$ (always a strictly positive quantity) and simplifying the term c_s^2, we obtain

$$\Delta t \leqslant \frac{h^2}{v + \sqrt{v^2 + c_s^2h^2}}. \tag{90}$$

Remark 12. In the limit of a vanishing artificial viscosity, the acoustic Courant–Friedrichs–Lewy condition is obtained, namely,

$$\Delta t \leqslant \frac{h}{c_s} \quad \text{or} \quad \sigma \leqslant 1. \tag{91}$$

Remark 13. In the limit of a vanishing speed of sound (condition very often encountered in hypervelocity impact problems), the stability limit is uniquely dependent on the artificial viscosity v and takes the classical form of the dissipative Courant–Friedrichs–Lewy condition:

$$\Delta t \leqslant \frac{h^2}{2\nu} \quad \text{or} \quad \kappa \leqslant \frac{1}{2}. \tag{92}$$

Remark 14. The predictor multi-corrector approach can also be interpreted as a fixed-point iteration procedure [18]. A sufficient condition for the convergence (in spectral space) of such procedure is $\|\boldsymbol{B}_1\| < 1$, that is $\rho(\boldsymbol{B}_1) < 1$. It is not difficult to verify that, when $\beta_k = \pi$, this condition coincides with (88).

7. The case of non-vanishing viscosity

Artificial viscosity operators are usually added in shock hydrodynamics computations to enhance the robustness of the algorithms under extreme shock wave conditions. Viscosity operators usually are modeled as Laplace diffusive operators, and may pose additional constraints on stability, further limiting the time step. In this case, because of the parabolic nature of the problem, the dispersion error analysis is less relevant and is omitted. Also, only results for the conservative scheme are presented, since this method is the main focus of the present work.

7.1. Amplification factor

The amplification factor (spectral radius) of the matrices $\boldsymbol{G}^{(i)}$ is presented as a function of the non-dimensional wave number β_k and acoustic Courant number σ in Fig. 2(c), (f), (i), (l), and (o), for a value of the non-dimensional viscosity coefficient $\kappa = 1/4$. A comparison with the plots in Fig. 2 for the case of $\kappa = 0$ shows that the introduction of diffusion in the proposed predictor/multi-corrector algorithm further restricts the stability range of the even iterates but provides a stability range for the otherwise unstable odd iterates. This fact can more clearly be observed in Figs. 8 and 9. Recalling that, by definition and

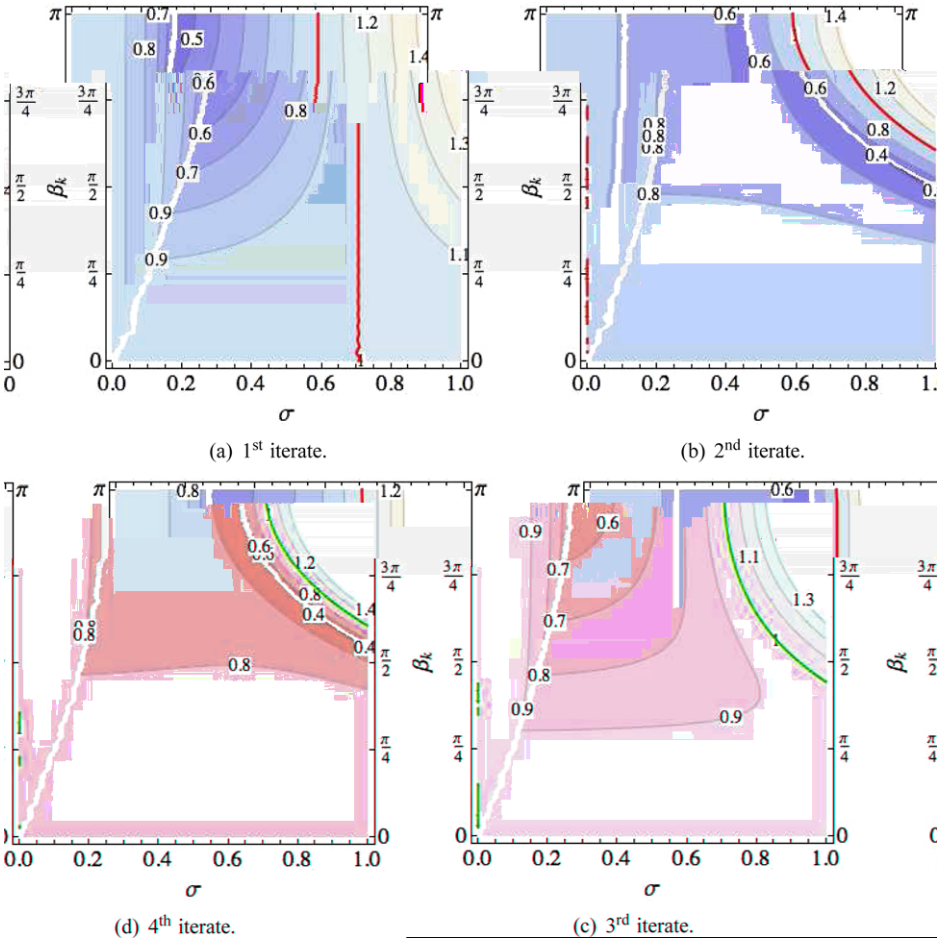

Fig. 8. Contour plots of the spectral radii for various predictor/multi-corrector iterates of the conservative algorithm, in the case $\kappa = 1/4$. The red continuous line correspond to the isoline for the spectral radius equal to unity. (For interpretation of the references to colour in this figure legend, the reader is referred to the web version of this article.)

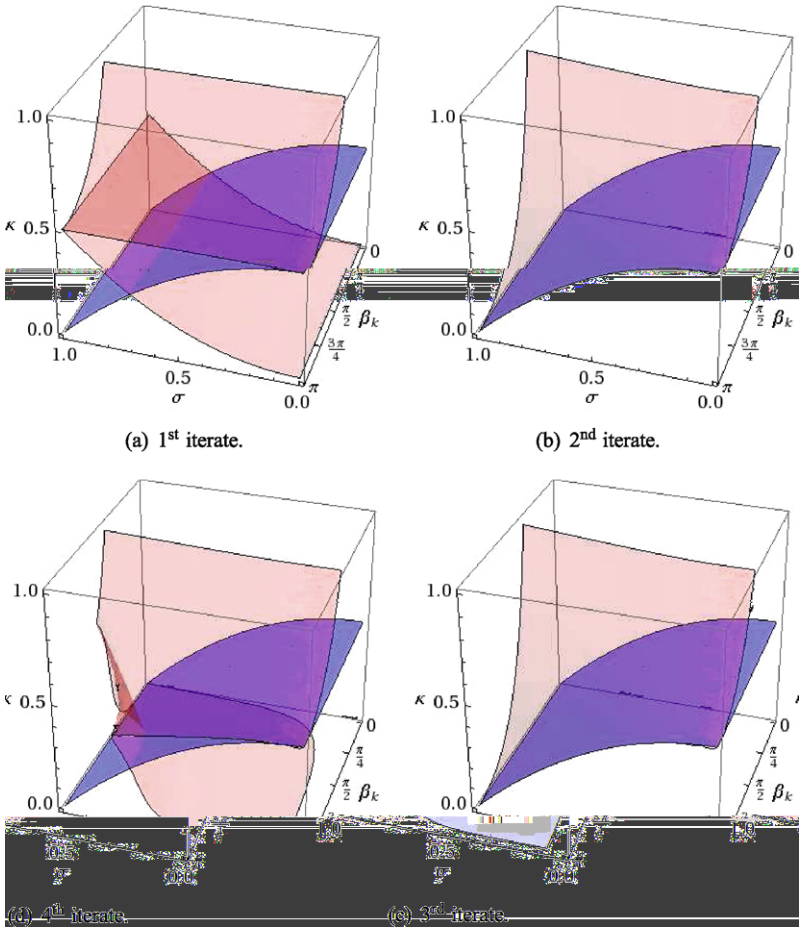

Fig. 11. Three-dimensional (red) surfaces representing the loci of the spectral radii equal to unity for the first four iterates of the conservative predictor/multi-corrector scheme. The blue surfaces represent the stability limit given by (88) (or, equivalently, (90)). (For interpretation of the references to colour in this figure legend, the reader is referred to the web version of this article.)

8.1. Periodic breaking wave

An interesting numerical test is represented by a breaking wave problem similar to the one described in [7,8]. The domain of the problem is the interval [0,1], subdivided into 200 elements, with periodic boundary conditions. The material is a γ-law ideal gas [14] with $\gamma = 5/3$. The initial density has a sinusoidal variation

$$\rho(x,0) = 0.001(1.0 + 0.1\sin(2\pi x)).$$

The initial pressure is

$$p(x,0) = 10^6\left(\frac{\rho(x,0)}{0.001}\right)^{\gamma},$$

and the initial velocity is

$$v(x,0) = 2\frac{(c_{s_0} - c_s)}{\gamma - 1},$$

where

$$c_s = \left(\gamma\frac{p(x,0)}{\rho(x,0)}\right)^{1/2},$$

and

$$c_{s_0} = \left(\gamma\frac{10^6}{0.001}\right)^{1/2}.$$

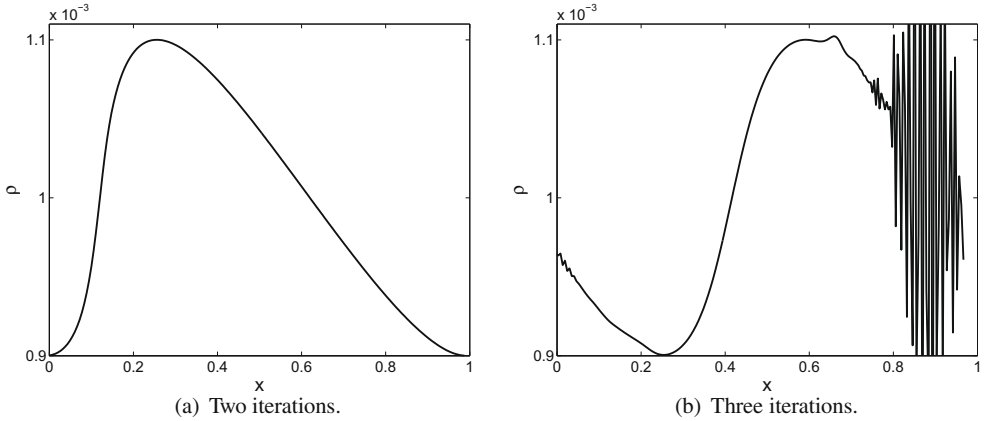

(a) Two iterations. (b) Three iterations.

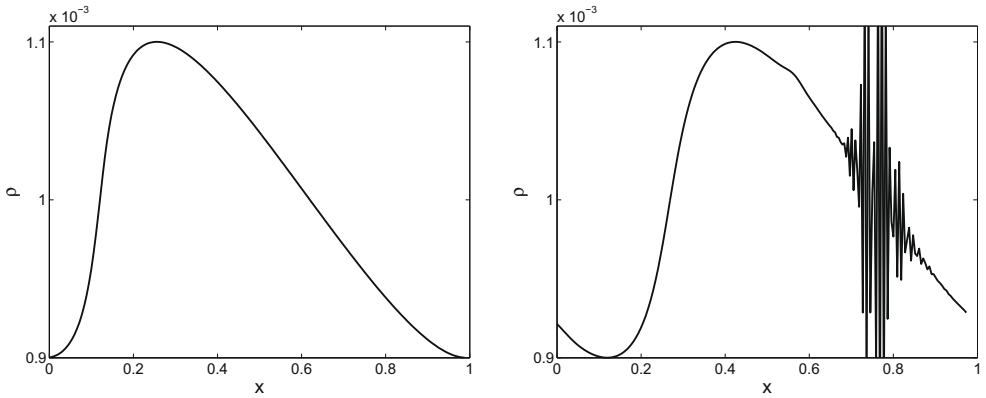

(c) Four iterations. (d) Five iterations.

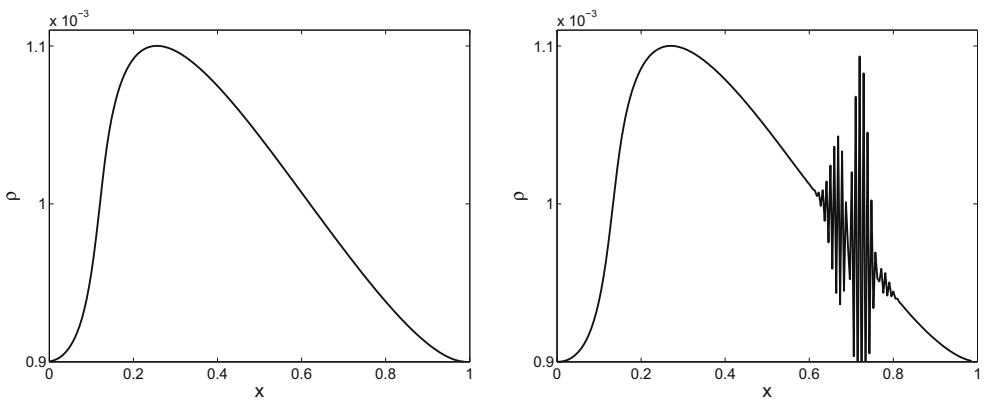

(e) Six iterations. (f) Seven iterations.

Fig. 12. Density versus spatial position at time 2.124×10^{-5} for the periodic breaking wave test problem. Solutions for different number of iterations of the predictor/multi-corrector algorithm are computed with no artificial viscosity and $CFL = 0.90$.

The solution is smooth for a finite time $0 < T_{\text{break}} < \infty$, at which point the wave breaks and a shock forms [7,8]. The nonlinear version of the present algorithm, described in detail in [17,18], is used. The results of Fig. 12 are obtained for several predictor/multi-corrector iterates, with no viscosity applied. The results of Fig. 13 are obtained with coefficients for the linear and quadratic part of the nonlinear artificial viscosity chosen as $c_1 = 0.15$ and $c_2 = 2.0$, respectively. All simulations were run using $CFL = 0.90$, that is, according to (90),

$$\Delta t \leqslant 0.90 \frac{h}{c_s}, \tag{94}$$

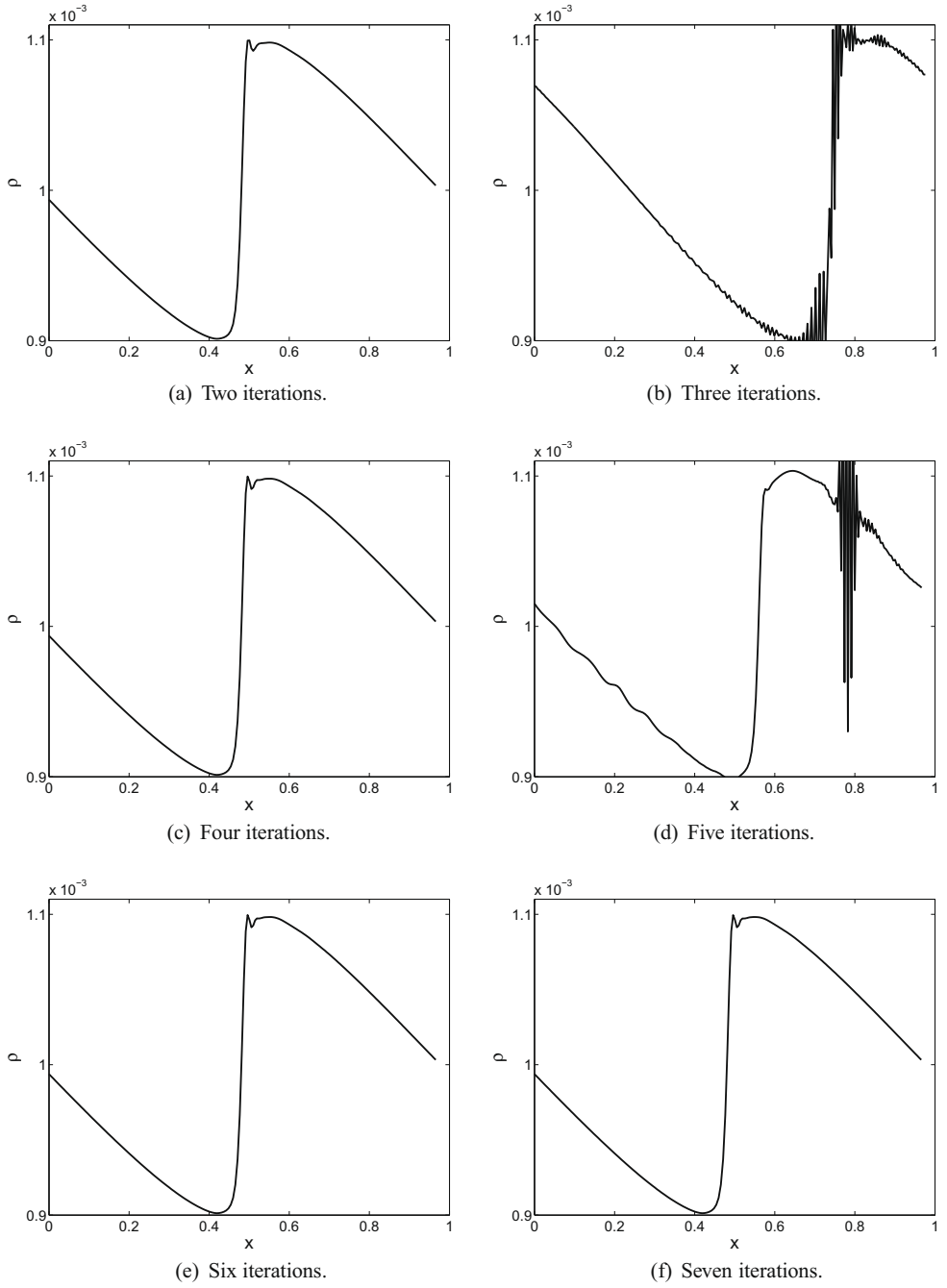

(a) Two iterations. (b) Three iterations.

(c) Four iterations. (d) Five iterations.

(e) Six iterations. (f) Seven iterations.

Fig. 13. Density versus spatial position at time 3.728×10^{-5} for the periodic breaking wave test problem. Solutions for different number of iterations of the predictor/multi-corrector algorithm are computed with active artificial viscosity in compression, and $CFL = 0.90$.

for the computations presented in Fig. 12, and

$$\Delta t \leqslant 0.90 \frac{h^2}{v + \sqrt{v^2 + c_s^2 h^2}}, \tag{95}$$

for the computations presented in Fig. 13 (note that the artificial viscosity v is applied only in compression, when $\mathbf{V}_{\boldsymbol{x}} \cdot \boldsymbol{v} < 0$). Consistent with the preceding analysis, an even number of iterations appears to be stable, and an odd number of iterations produces obviously unstable results when no artificial viscosity is applied. In particular, Figs. 12 and 13 show the onset of

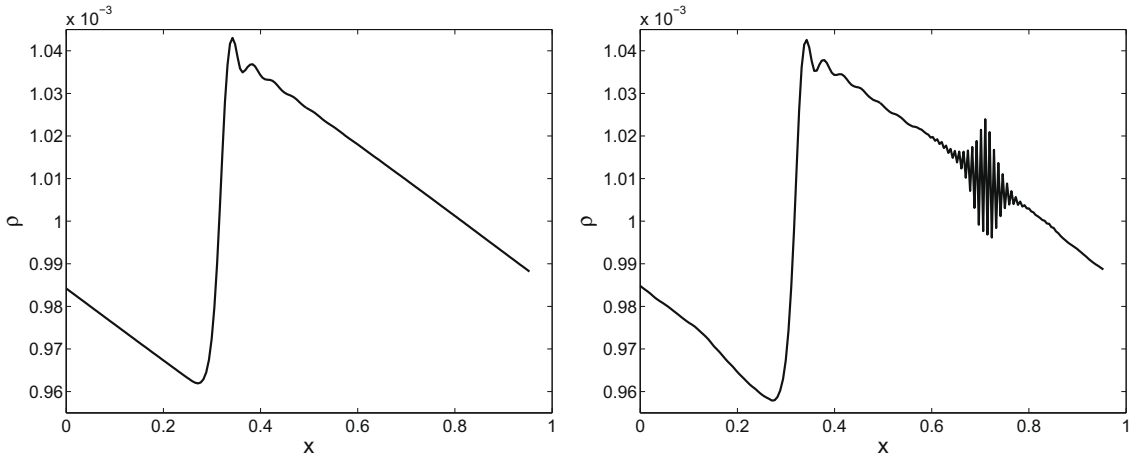

(a) Two iterations. (b) Seven iterations.

Fig. 14. Density versus spatial position at time 1.87327×10^{-4} for the periodic breaking wave test problem. Fig. 14(a) shows the stable solution in the case of two iterations. Fig. 14(b) shows the onset of instabilities for seven iterations. Solutions are computed with artificial viscosity active in compression and $CFL = 0.90$.

instabilities, which completely overwhelm the numerical results as the computations proceed for longer times. Stability is seemingly regained in the case of seven iterations when the artificial viscosity is active, at the time $t = 3.728 \times 10^{-5}$ under consideration. However, at the later time $t = 1.87327 \times 10^{-4}$, the case of seven iterations is clearly unstable (see Fig. 14).

This overall behavior is the result of the convergence of the predictor/multi-corrector algorithm to the neutrally-stable implicit limit, in combination with the dissipation due to the artificial viscosity in compression regions. Figs. 4 and 10 and Eqs. (75)–(82)) show that the amplification factor of the odd iterates decreases for an increasing number of iterations, consequently reducing the growth rate of instabilities. The subsequence of odd iteration simulations does converge to a stable solution in the limit of an infinite number of iterations. The magnitude of the instability decreases with increasing iterations, but the instability never vanishes completely for a finite number of iterations. The issue may not always be visibly apparent in the results of a simulation if many iterations are used for a short time interval. In some circumstances, increasing the simulation time allows the inherent instability to clearly manifest itself. This is the behavior observed when the breaking wave problem is run for a longer time (again see Fig. 14).

Remark 16. As already discussed, the algorithm under investigation is second-order accurate for two or more iterations. While, from a point of view of accuracy, no more than two iterations are required, it was often found by the authors that, in more challenging computations, a larger number of iterations was required to minimize the occurrence of shock over/undershoots in the solution [17,18]. This point, in our view, justifies the presentation of a detailed analysis for a number of iterations larger than two.

8.2. Interacting blast waves

As a second numerical test, we consider the Woodward-Colella interacting shock wave test problem [23]. In one dimension the domain of the problem is the interval [0,1], subdivided into 400 elements. Again, the material is a γ-law ideal gas with $\gamma = 1.4$. The gas is initially at rest between reflecting walls, with a uniform initial density everywhere equal to 1. On the subdomain [0,0.1] the initial pressure is 1000 and on the subdomain [0.9,1.0] the initial pressure is 100. Everywhere else the pressure is initialized to 0.01. Two strong shock waves develop and interact. The linear and quadratic part of the nonlinear artificial viscosity have coefficients $c_1 = 0.15$ and $c_2 = 2.0$, respectively. Fig. 15 plots the numerical results of density versus position for various values of the *CFL* control parameter. Two predictor/corrector iterations are used for these simulations. The simulations with $CFL \leqslant 1$ do not show any sign of instability, while the simulations with $CFL > 1.10$ appear mildly unstable. The time-step stability estimate seems to be accurate (and more restrictive) to within about 10%, at least for this test problem.

Remark 17. This added stability may be due to the conservation properties enjoyed by the algorithm in the nonlinear setting, which bound the global total energy to stay constant throughout the computation.

Remark 18. The large spurious overshoot in density at $x \approx 0.765$ is typical of Lagrangian simulations of this test [12,16], and is a somewhat expected feature in this computation.

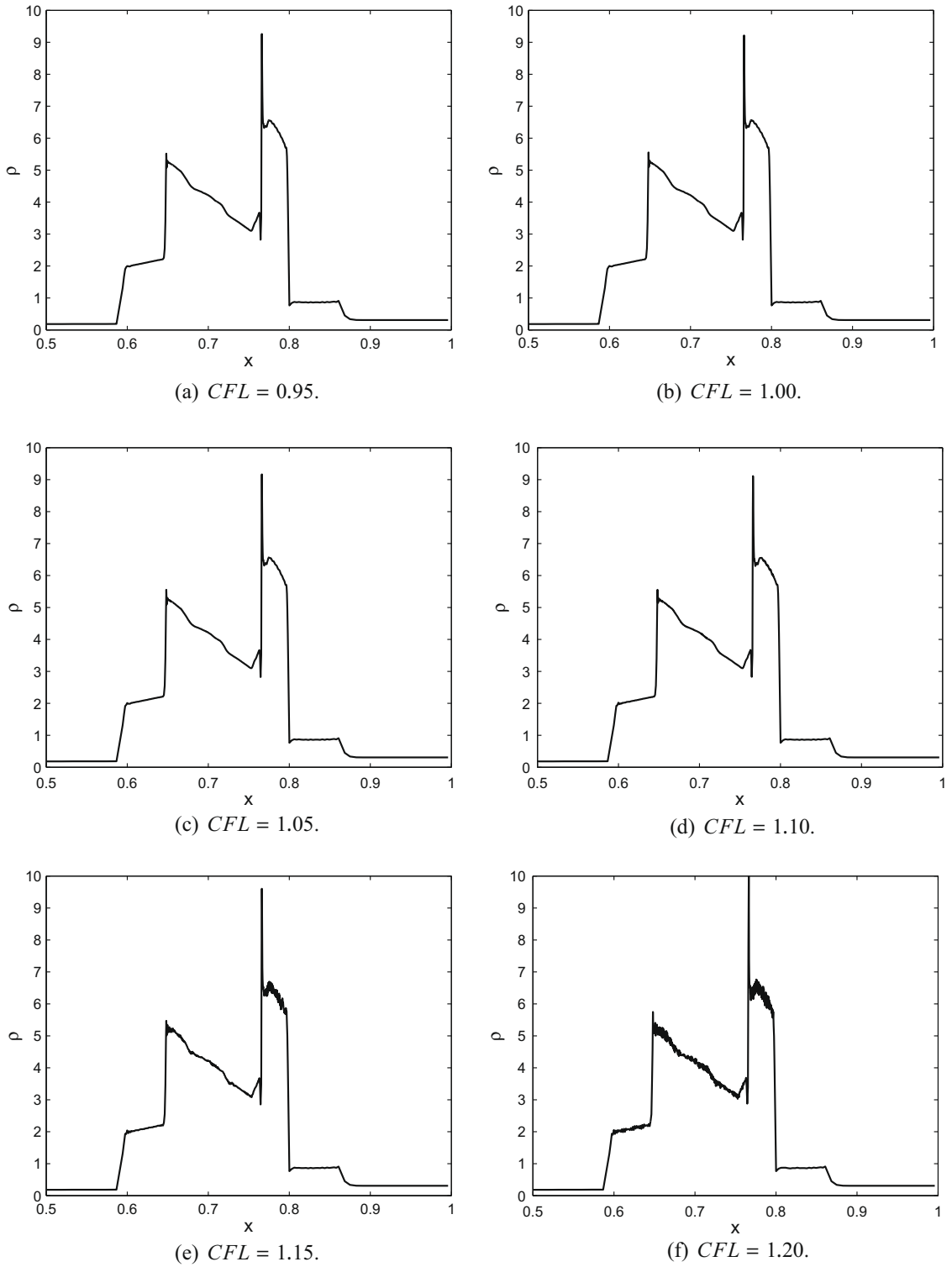

(a) $CFL = 0.95$. (b) $CFL = 1.00$.

(c) $CFL = 1.05$. (d) $CFL = 1.10$.

(e) $CFL = 1.15$. (f) $CFL = 1.20$.

Fig. 15. Density versus spatial position for the Woodward–Colella test problem for different values of the *CFL* parameter. Plots are at the final time of 0.038.

9. Summary

We have presented a von Neumann stability analysis of a linearized version of the predictor/multi-corrector algorithm proposed in [17,18], which, at least in the one-dimensional setting, coincides with the time integrators documented in

[2,5]. We have highlighted as a curious feature of this algorithm, that the odd iterates are unconditionally unstable, while the even are conditionally stable (at least up to four iterates). Numerical tests showed that the time-step stability bound derived in the linearized analysis also works well in the nonlinear case, and that the instabilities predicted in the linearized analysis do occur in nonlinear computations.

Acknowledgments

The authors would like to thank, for very valuable discussion, Professor T.J.R. Hughes at the University of Texas in Austin, Dr. M. Shashkov and Dr. B. Wendroff at Los Alamos National Laboratory, and Dr. J. Carpenter, Dr. C. Ober, Dr. T. Voth, Dr. V.G. Weirs, and Dr. M. Wong at Sandia National Laboratories. The authors would also like to thank Dr. R. Summers and Dr. S. Collis, at Sandia National Laboratories, for support and encouragement during the development of this research work.

References

[1] M.L. Abell, J.P. Braselton, Mathematica by Example, fourth ed., Academic Press, 2008.
[2] A. Barlow, A compatible finite element multi-material ALE hydrodynamics algorithm, International Journal for Numerical Methods in Fluids 56 (8) (2008) 953–964.
[3] A.L. Bauer, D.E. Burton, E.J. Caramana, R. Loubère, M.J. Shashkov, P.P. Whalen, The internal consistency, stability, and accuracy of the discrete, compatible formulation of Lagrangian hydrodynamics, Journal of Computational Physics 218 (2) (2006) 572–593.
[4] A.L. Bauer, R. Loubère, B. Wendroff, On stability of staggered schemes, SIAM Journal on Numerical Analysis 46 (2) (2008) 996–1011.
[5] E.J. Caramana, M.J. Shashkov, P.P. Whalen, Formulations of artificial viscosity for multi-dimensional shock wave computations, Journal of Computational Physics 144 (1998) 70–97.
[6] B.D. Coleman, V.J. Mizel, Existence of caloric equations of state in thermodynamics, The Journal of Chemical Physics 40 (4) (1964) 1116–1125.
[7] A.W. Cook, W.H. Cabot, A High-wavenumber Viscosity for High-resolution Numerical Methods, Technical Report UCRL-ID-152002, Lawrence Livermore National Laboratory, Livermore, CA, 2003.
[8] A.W. Cook, W.H. Cabot, A high-wavenumber viscosity for high-resolution numerical methods, Journal of Computational Physics 195 (2) (2004) 594–601.
[9] A. Curnier, Computational Methods in Solid Mechanics, Kluwer Academic Press, Amsterdam, 1994.
[10] D.L. Hicks, Stability analysis of WONDY (a hydrocode based on artificial viscosity method of von Neumann and Richtmyer) for a special case of Maxwell's law, Mathematics of Computation 32 (144) (1978) 1123–1130.
[11] R.A. Horn, C.R. Johnson, Matrix Analysis, Cambridge University Press, Cambridge, UK, 1985.
[12] R. Loubère, M.J. Shashkov, A subcell remapping method on staggered polygonal grids for arbitrary-Lagrangian Eulerian methods, Journal of Computational Physics 209 (1) (2005) 105–138.
[13] E. Love, G. Scovazzi, W.J. Rider, Algorithmic Properties of the Midpoint Predictor/corrector Time Integrator, Technical Report, SAND2009-1127, Sandia National Laboratories, New Mexico, March 2009. <http://www.cs.sandia.gov/ALEGRA/Alegra_Home.html>.
[14] R. Menikoff, B.J. Plohr, The Riemann problem for fluid flow of real materials, Reviews of Modern Physics 61 (1) (1989) 75–130.
[15] A.R. Mitchell, D.F. Griffiths, The Finite Difference Method in Partial Differential Equation, John Wiley, London, 1980.
[16] R.B. Pember, R.W. Anderson, Comparison of Staggered-mesh Lagrange Plus Remap and Cell-centered Direct Eulerian Godunov Schemes for Eulerian Shock Hydrodynamics, Technical Report UCRL-JC-139820, Lawrence Livermore National Laboratory, Livermore, CA, November 2000.
[17] G. Scovazzi, E. Love, M.J. Shashkov, A Multi-scale Q1/P0 Approach to Lagrangian Shock Hydrodynamics, Technical Report, SAND2007-1423, Sandia National Laboratories, New Mexico, March 2007. <http://www.cs.sandia.gov/gscovaz/pubs.html>.
[18] G. Scovazzi, E. Love, M.J. Shashkov, A multi-scale Q1/P0 approach to Lagrangian shock hydrodynamics, Computer Methods in Applied Mechanics and Engineering 197 (9–12) (2008) 1056–1079.
[19] G. Scovazzi, J.N. Shadid, E. Love, T.J.R. Hughes, Stabilized Shock Hydrodynamics: IV. Computations with a Conservative Updated Lagrangian Method, Technical Report, SAND2009-1523J, Sandia National Laboratories, New Mexico, 2009. <http://www.cs.sandia.gov/gscovaz/pubs.html>.
[20] J.C. Strikwerda, Finite Difference Schemes and Partial Differential Equations, Chapman & Hall, New York, 1989.
[21] J. von Neumann, R.D. Richtmyer, A method for the numerical computation of hydrodynamic shocks, Journal of Applied Physics 21 (1950) 232–237.
[22] S. Wolfram, The Mathematica Book, fourth ed., Cambridge University Press, 1999.
[23] P.R. Woodward, P. Colella, The numerical simulation of two-dimensional fluid flow with strong shocks, Journal of Computational Physics 54 (1984) 115–173.